

Constructing Efficient and Stable Perovskite Solar Cells via Interconnecting Perovskite Grains

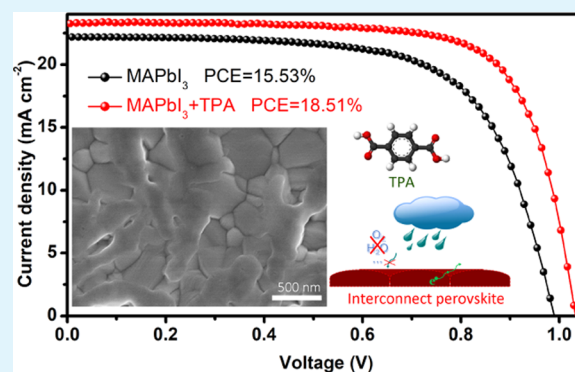
Xian Hou,[†] Sumei Huang,[†] Wei Ou-Yang,[†] Likun Pan,[‡] Zhuo Sun,[†] and Xiaohong Chen^{*,†}

[†]Engineering Research Center for Nanophotonics & Advanced Instrument, Ministry of Education, School of Physics and Materials Science and [‡]Shanghai Key Laboratory of Magnetic Resonance, School of Physics and Materials Science, East China Normal University, Shanghai 200062, China

Supporting Information

ABSTRACT: A high-quality perovskite film with interconnected perovskite grains was obtained by incorporating terephthalic acid (TPA) additive into the perovskite precursor solution. The presence of TPA changed the crystallization kinetics of the perovskite film and promoted lateral growth of grains in the vicinity of crystal boundaries. As a result, sheet-shaped perovskite was formed and covered onto the bottom grains, which made some adjacent grains partly merge together to form grains-interconnected perovskite film. Perovskite solar cells (PSCs) with TPA additive exhibited a power conversion efficiency (PCE) of 18.51% with less hysteresis, which is obviously higher than that of pristine cells (15.53%). PSCs without and with TPA additive retain 18 and 51% of the initial PCE value, respectively, aging for 35 days exposed to relative humidity 30% in air without encapsulation. Furthermore, MAPbI₃ film with TPA additive shows superior thermal stability to the pristine one under 100 °C baking. The results indicate that the presence of TPA in perovskite film can greatly improve the performance of PSCs as well as their moisture resistance and thermal stability.

KEYWORDS: perovskite solar cells, terephthalic acid, interconnection, efficiency, stability



INTRODUCTION

Organic–inorganic metal halide perovskites have attracted enormous attention to photovoltaic technologies due to the high-performance and low-cost solution-based fabrication routes.^{1–4} The growth in efficiencies of perovskite solar cells (PSCs) has been unprecedentedly rapid,^{5–8} and a world record power conversion efficiency (PCE) of 22.1% was achieved in 2016.⁹ Crucially, accurate control over the morphology and electronic properties of perovskite layer and the device architecture play important roles to achieve high-performance and stable PSCs.¹⁰ However, like most ionic materials, the organic–inorganic metal halide perovskite has a reasonable quantity of noncoordinated ions, especially the I[−] anions can rather easily migrate into perovskite grains¹¹ and even further migrate out of the perovskite layer and corrode the metal electrode, which can form a lot of defects in the perovskite layer and accelerate the deterioration of perovskite film.¹² These defects are more easily formed at the surfaces and grain boundaries of perovskite film, which can act as nonradiative recombination centers, reducing the charge carrier lifetime and thus decreasing the power conversion efficiency (PCE) of PSCs.¹³ On the other hand, defects-formed regions and grain boundaries are easily attacked by corrosive moisture or oxygen, promoting the disintegration of perovskite film.^{14,15} Therefore, developing a high-quality perovskite film with expected merits, including proper stoichiometry, full surface coverage, large

grain size, and less grain boundaries, can reduce the bulk defect density and carrier recombination and thus improve the PCE and stability of PSCs.

Many efforts have been made to obtain high-quality perovskite film. Grain size, crystallinity, and surface coverage of perovskite films can be greatly improved by solvent engineering,⁶ solvent annealing,¹⁶ gas treatment,^{17,18} Ostwald ripening,¹⁹ and incorporating additives.²⁰ Among these methods, incorporating additives plays an important role in assisting perovskite crystal growth for improving the PCE and stability of PSCs. Li et al. introduced butylphosphonic acid 4-ammonium chloride into the neighboring perovskite grains, which greatly improved the moisture resistance of PSCs because the hydrogen-bonding interaction promoted grain growth.²¹ Coincidentally, 2-aminoethanethiol was used as a ligand to bridge methylammonium iodide (MAI) and PbI₂, which realized the synchronous growth environment of MAI and PbI₂ crystals and formed a compact and stable perovskite film.²² Besides, poly(methyl methacrylate),²³ poly(ethylene glycol),²⁴ 1,3:2,4-di-O-methylbenzylidene-D-sorbitol,²⁵ and many other additives were incorporated into perovskite films, which also achieved large grain size and stability due to the

Received: June 13, 2017

Accepted: September 22, 2017

Published: September 22, 2017

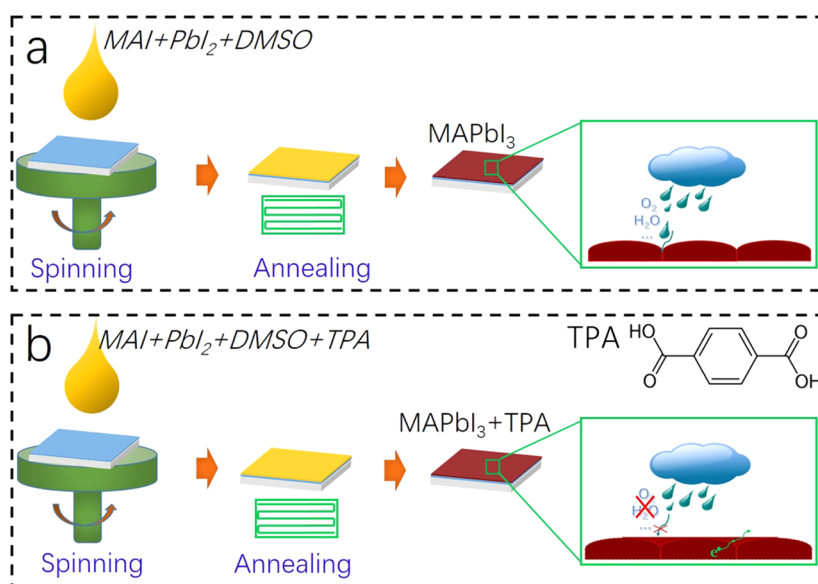


Figure 1. Schematic procedure for the preparation of MAPbI₃ (a) and MAPbI₃ + TPA (b) films.

“cross-link” or chelation effects between the perovskite grains and functional groups. In these typical additives, functional groups, such as hydroxyl group (–OH), carboxyl group (–COOH), and ammonium group (–NH₂), were linked with flexible carbon chain, which usually interacts with Pb ions or I ions of perovskite and changes the crystallization process of perovskite grains. Concomitantly, hydrogen bonds of these groups can effectively suppress the migration of ions in perovskite film, which may reduce the hysteresis and improve the stability of PSCs.²⁶

Although there are great achievements in improving the crystallization process to get high-quality perovskite films possessing uniform morphology and large grain size by incorporating additives into perovskite, previous reported works are mostly devoted to the flexible molecular cross-link or chelation with perovskite to increase the perovskite grain size and smoothen the morphology of perovskite film.^{21–24} The exposed grain boundaries are still a key scientific challenge to get high-performance and long-term stable PSCs because the grain boundaries are highly susceptible to moisture and oxygen.^{27,28}

To remedy the exposed grain boundaries of perovskite film, terephthalic acid (TPA) as an additive was first incorporated into perovskite precursor solution, where the rigid benzene ring is linked to two carboxyl groups at 1,4-symmetrical position. Benzene ring has a high cohesive energy²⁹ compared to the previously reported flexible carbon-chain-based additives due to its rigidity properties and the strong interaction of π – π bonds, which make TPA easily gather at the vicinity of perovskite grain boundaries and grain surface during film formation. The gathered TPA molecules at grain boundaries can act as templates³⁰ and possibly promote the lateral growth of perovskite grains in grain boundaries because of the heterogeneous nucleation lowering the nucleation free-energy barrier in the grain boundaries.³¹ The formed sheet-shaped perovskite remedied some exposed grain boundaries and were covered onto the bottom grains, which can partly merge adjacent grains to form interconnected perovskite grains. Simultaneously, the strong coordination between I[–] and hydrogen bonds of hydroxyl groups in TPA can suppress the

ion migration of perovskite. As a result, PSCs with TPA additive exhibited a PCE of more than 18.5% with robust moisture resistance and thermal stability, which is obviously superior to that of pristine PSCs.

■ MATERIALS AND METHODS

Materials. All of the reagents and materials were commercially available and used without purification. Fluorine-doped tin oxide (FTO) glass (thickness: 2.2 mm, sheet resistance: 14 Ω/\square) was purchased from Nippon Sheet Glass, Japan. Lead(II) iodide (PbI₂, 99.9%), lithium-bis(trifluoromethanesulfonyl)imide (Li-TFSI, 98%), and 4-*tert*-butylpyridine (TBP, 98%) were purchased from Aladdin Reagents. CH₃NH₃I (MAI) was purchased from 1-Material-Organic Nano Electronic (1-Material Inc.). TiO₂ paste (Dyesol 18-NRT) was purchased from Dyesol Company. 2,2',7,7'-Tetrakis(*N,N*-di-*p*-methoxy-phenylamine)-9,9'-spirobifluorene (spiro-OMeTAD, $\geq 99\%$) was purchased from Xi'an Polymer Light Technology Corp., Xi'an, China.

Cell Fabrication. A compact TiO₂ layer with 40 nm thickness was first spin-coated on a pre-cleaned FTO substrate. Then, a mesoporous TiO₂ layer was deposited on top of the compact TiO₂ layer by spin-coating TiO₂ paste (Dyesol 18-NRT, diluted with ethanol at 1:6 by weight) at 4000 rpm for 30 s, followed by annealing at 500 °C for 30 min in air. Finally, the substrate was immersed into 40 mM TiCl₄ aqueous solution for 30 min at 70 °C and washed with deionized water and ethanol, followed by annealing at 500 °C for 30 min in air. The perovskite layer was spin-coated on the TiO₂ layer via a solvent-modified engineering-assisted one-step spin-coating procedure. Specifically, 30 μ L of premixed solution containing 159 mg of MAI, 462 mg of PbI₂, 78 mg of dimethyl sulfoxide (DMSO), 600 mg of dimethylformamide, and a certain amount of TPA was dropped on the substrate and then the substrate was spun at 4000 rpm for 40 s. Within the first 6 s of spinning, 0.5 mL of anhydrous diethyl ether was continuously dropped on the substrate. Then, the substrates were heated at 100 °C for 10 min. After cooling to room temperature, the mixture solution containing 72.3 mg of spiro-OMeTAD, 28.8 μ L of TBP, and 17.5 μ L of Li-TFSI in acetonitrile (520 mg mL^{–1}) was dissolved in 1 mL of chlorobenzene and then spin-coated onto the perovskite layer to form a 60 nm thick hole transport layer (HTL). Finally, an 80 nm thick Ag/Al alloy electrode was thermally evaporated onto the spiro-OMeTAD layer.

Characterization. The morphology and structure of samples were, respectively, investigated by scanning electron microscopy (SEM, Hitachi S-4800) and X-ray diffraction (XRD, Holland Analytical PRO

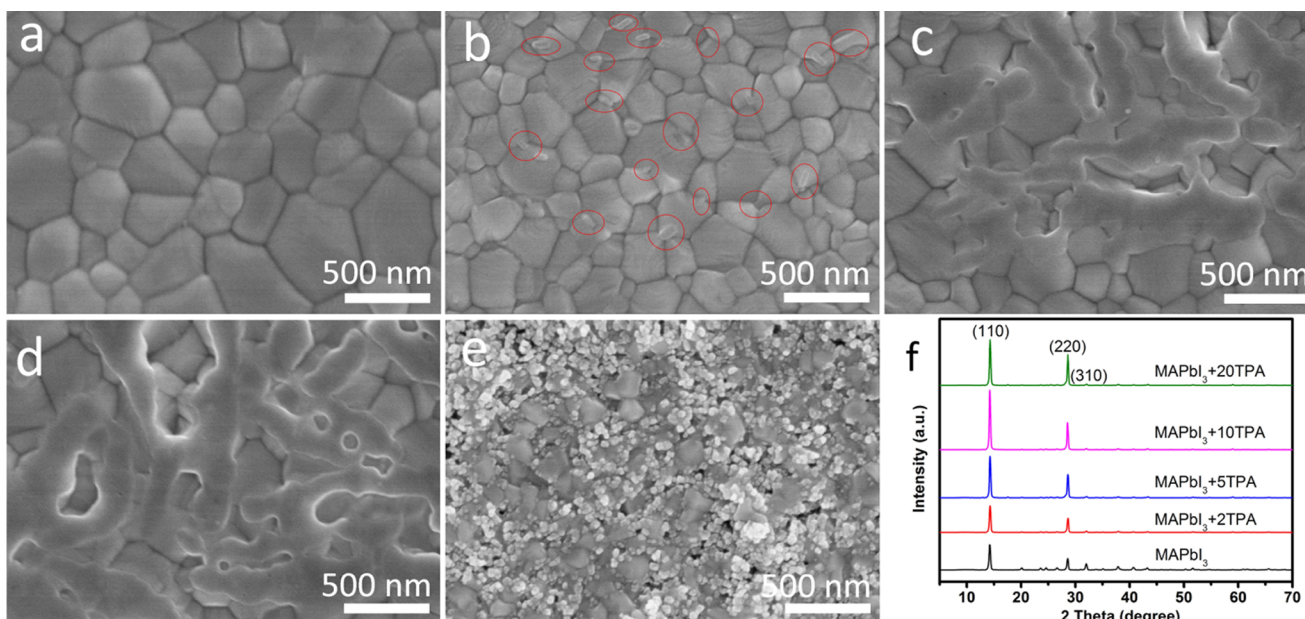


Figure 2. Top view SEM images of MAPbI₃ films without (a) and with (b) 2, (c) 5, (d) 10, and (e) 20 mg mL⁻¹ TPA additive. (f) XRD patterns of perovskite films.

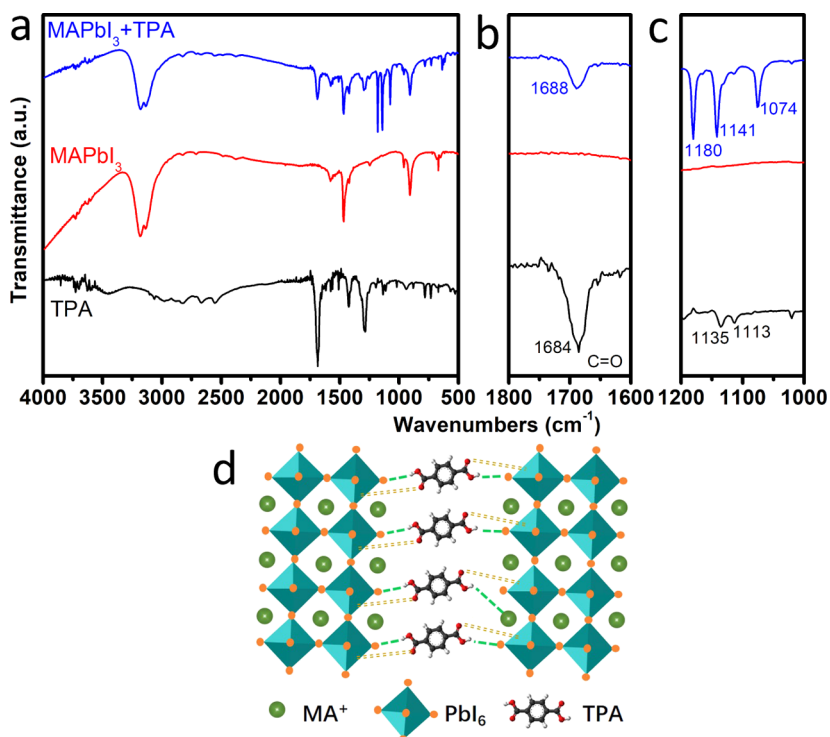


Figure 3. (a) FTIR spectra of TPA, pristine MAPbI₃ film, and MAPbI₃ + TPA film. (b, c) Magnification spectra from the part wavenumbers of (a). (d) Representation of the interaction between perovskite and TPA.

PW3040/60) with Cu K α radiation ($V = 30$ kV, $I = 25$ mA). Light absorption spectra were measured using a UV-vis spectrophotometer (Hitachi U-3900). IR spectra were measured using a Bruker Vertex 80v Fourier transform infrared spectrometer. The photocurrent density-voltage ($J-V$) curve was measured using a Keithley model 2440 SourceMeter under the illumination of AM 1.5 G and 100 mW cm⁻² simulated solar light from a Newport solar simulator system. During the photovoltaic measurements, all devices were covered with a mask to define the active area of 0.10 cm². The incident photon-to-current conversion efficiency (IPCE) was measured using a Newport Optical Power Meter 2936-R controlled by TracQ Basic software.

RESULTS AND DISCUSSION

MAPbI₃ films were prepared using a one-step spin-coating method, as shown in the schematic of Figure 1. Briefly, MAPbI₃ precursor (MAI/PbI₂/DMSO = 1:1:1, mole ratio) solutions containing different amounts of TPA additives (0, 2, 5, 10, and 20 mg mL⁻¹) were spin-coated onto the mesoporous TiO₂ scaffold layer individually. Figure 2a–e shows the top view scanning electron microscopy (SEM) images of MAPbI₃ films with different concentrations of TPA additive. The pristine

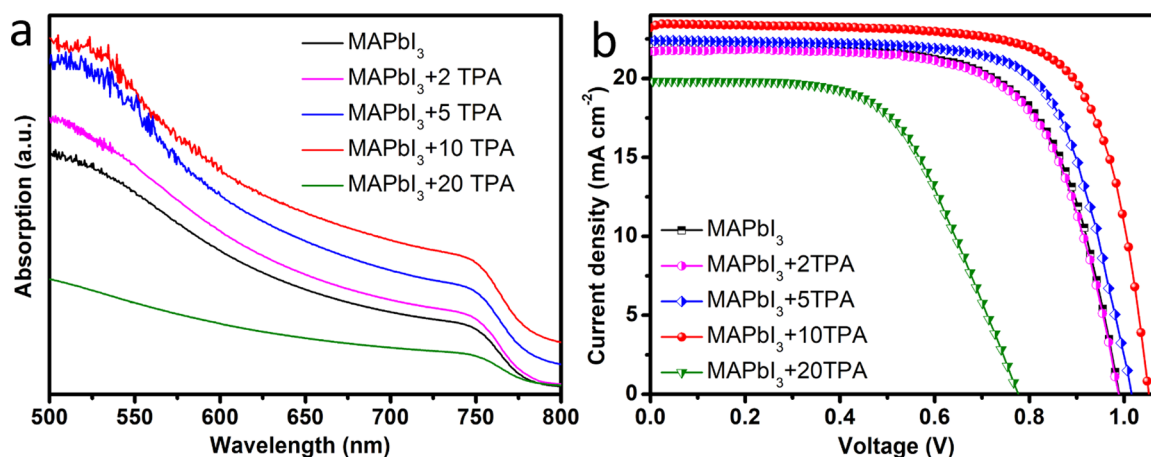


Figure 4. (a) UV-vis absorption spectra of perovskite films with different concentrations of TPA additive. (b) J - V curves of PSCs measured with AM 1.5 G irradiation at 100 mW cm^{-2} simulated solar light.

MAPbI₃ grain sizes are about 300–800 nm, and the grain boundaries can be clearly observed, which is consistent with the previously reported morphology of MAPbI₃ film prepared by one-step method.³² However, the surface morphologies of MAPbI₃ films with TPA additive have another vision. Due to the rigidity property caused by benzene ring in TPA, the high cohesive energy makes TPA easily gather in the vicinity of perovskite grain boundaries during film formation. The gathered TPA molecules at grain boundaries can serve as a support template³⁰ and induce perovskite nucleation with lateral growth in grain boundaries because the heterogeneous nucleation can obviously lower the nucleation free-energy barrier in the grain boundaries.³¹ Thus, some small bar-shaped grains were formed in the vicinity of crystal boundaries and bridged the two sides of bottom perovskite grains after adding 2 mg mL^{-1} TPA, as shown in the red circles in Figure 2b. However, the grain sizes of perovskite film with 2 mg mL^{-1} TPA were slightly reduced because TPA can provide more nucleation sites. By further increasing the TPA concentration to 5 – 10 mg mL^{-1} , the abundant nucleation sites caused by TPA promote the bar-shaped bridges grown up to sheet-shaped grains, which can partly remedy the exposed grain boundaries, and some bottom grains are merged into interconnected perovskite communities. However, a coarse perovskite film with a lot of small perovskite grains surrounding the original perovskite grains was formed after further increasing the TPA concentration to 20 mg mL^{-1} , as shown in Figure 2e. The excessive nucleation sites of TPA along the grain boundaries are responsible for the formation of small perovskite grains, which further supports the fact that the TPA molecules are easily segregated in the vicinity of grain boundaries.

Fourier transform infrared (FTIR) transmission spectra of TPA, MAPbI₃, and MAPbI₃ + TPA films were collected to verify the interactions between TPA and perovskite, as shown in Figure 3a. The C=O vibration band of TPA in perovskite film was moved to 1688 from 1684 cm^{-1} , as shown in Figure 3b, which is attributed to coordinate effects between the oxygen lone pairs of -COOH group and Pb ions of perovskite.²⁶ In addition, three emerging peaks at 1180 , 1141 , and 1074 cm^{-1} were observed, as shown in Figure 3c. Although the formation factors of these three peaks need to be investigated in the future, this result can confirm that TPA molecules have strongly interacted with perovskite grains, which is expected to affect the crystallization process and the morphology of perovskite layer.

The conceivable interactions between perovskite and TPA are further shown in Figure 3d.

X-ray diffraction (XRD) patterns were measured to evaluate the effect of TPA on perovskite crystallinity. XRD patterns of perovskite films with different concentrations of TPA additive are shown in Figure 2f. The clear diffraction peaks can be indexed to the (110), (220), and (310) diffraction of perovskite grains, respectively.²⁶ The absolute intensities of the (110) and (220) peaks of MAPbI₃ with TPA compared to pristine MAPbI₃ become stronger, implying that TPA additive can improve the crystallinity of perovskite.³³ Furthermore, the (310) peak of MAPbI₃ films with TPA additive become significantly weakened, suggesting that TPA additive can affect the growth direction of perovskite crystal.³⁴ However, the intensities of the (110) and (220) peaks for MAPbI₃ incorporated with 20 mg mL^{-1} TPA became lower than those of 10 mg mL^{-1} TPA additive, which is mainly caused by the inferior perovskite film with a lot of small grains.

To further investigate the crystallization of perovskite film with TPA additive, SEM images and XRD patterns of preperovskite film with and without TPA additive before annealing are shown in Figure S1. The more compact and rodlike morphology of the preperovskite film with TPA additive was observed from the SEM images. The relatively strong (110) peak of the perovskite film with TPA additive from XRD patterns suggests that TPA additive has good capability of inducing crystallization of perovskite film without further annealing. Antisolvents also play an important role in improving the crystallization of perovskite film.³⁵ Figure S2 shows SEM images and XRD patterns of perovskite films without antisolvent treatment but annealed at $100 \text{ }^\circ\text{C}$. The very strong peaks of perovskite films and the compact morphology without obvious cracks after incorporating TPA further suggest that TPA additive is an effective material to improve the compactness and crystallization of perovskite film without further antisolvent treatment.

Figure 4a presents the UV-vis absorption spectra of MAPbI₃ film without and with different concentrations of TPA additive. The light absorption intensities of perovskite films with TPA concentration increasing from 2 to 10 mg mL^{-1} were gradually enhanced due to the integrated effects of better crystallinity and larger sizes of perovskite grains. However, the light absorption of perovskite film with 20 mg mL^{-1} TPA additive was

deteriorated, which is attributed to the coarse perovskite film including a lot of small perovskite grains.

Figure S3a,b shows the cross-sectional SEM images of PSCs based on perovskite films without and with 10 mg mL⁻¹ TPA additive. Two types of perovskite films show similar thickness of ~500 nm. The *J*-*V* curves of PSCs with different concentrations of TPA under AM 1.5 G irradiation at 100 mW cm⁻² are shown in Figure 4b, and the relevant photovoltaic parameters are listed in Table 1. The pristine

Table 1. Photovoltaic Parameters of PSCs with Different TPA Concentrations

cells	V_{OC} (V)	J_{SC} (mA cm ⁻²)	FF (%)	PCE (%)
MAPbI ₃	0.99	22.09	71.02	15.53
MAPbI ₃ + 2TPA	0.99	21.68	68.12	14.62
MAPbI ₃ + 5TPA	1.02	22.51	69.77	16.02
MAPbI ₃ + 10TPA	1.05	23.49	75.06	18.51
MAPbI ₃ + 20TPA	0.78	19.83	57.59	8.91

MAPbI₃ PSCs show the best PCE of 15.53% with a V_{OC} of 0.99 V, J_{SC} of 22.09 mA cm⁻², and FF of 71.02%. After adding 2 mg mL⁻¹ TPA, the MAPbI₃ + 2TPA device shows a PCE of 14.62%, which is slightly lower than that of the pristine PSCs due to the decreased grain size. The performance of PSCs gradually improved with TPA concentration increasing from 5 to 10 mg mL⁻¹, and PSCs with 10 mg mL⁻¹ TPA additive

obtained the highest PCE of 18.51% with a V_{OC} of 1.05 V, J_{SC} of 23.49 mA cm⁻², and FF of 75.06%, indicating that incorporating proper amount TPA into MAPbI₃ can significantly improve the performance of PSCs. However, PSCs with 20 mg mL⁻¹ TPA additive were severely deteriorated due to the formation of a lot of small perovskite grains.

The characteristics of PSCs with 10 mg mL⁻¹ TPA were further investigated due to their superior performance, and they were named as MAPbI₃ + TPA cells. Anomalous hysteresis phenomenon through *J*-*V* testing was widely observed in PSCs. Previous results showed that this phenomenon is related to the properties of the perovskite layer and device configuration.² Because PSCs without and with TPA had the same contact materials and configurations, the differences derived only from the coverage and crystallinity of perovskite layers. The typical *J*-*V* curves of PSCs without and with TPA recorded at a scanning rate of 0.1 V s⁻¹ are shown in Figure 5a, and the detailed photovoltaic parameters are summarized in Table 2. The pristine MAPbI₃ PSCs showed PCE values of 15.53 and 12.96% under reverse and forward scanning, respectively, which yielded a difference of 16.54% in PCE values. By contrast, for PSCs with TPA additive, the reverse- and forward-scanning PCE values are 18.51 and 15.87%, respectively, showing weak hysteresis effect and yielding a PCE difference of 14.26%. The alleviated *J*-*V* hysteresis is mostly related to less traps and grain boundaries of TPA-induced MAPbI₃ film.³⁶ Besides, the carboxyl of TPA can help to hold

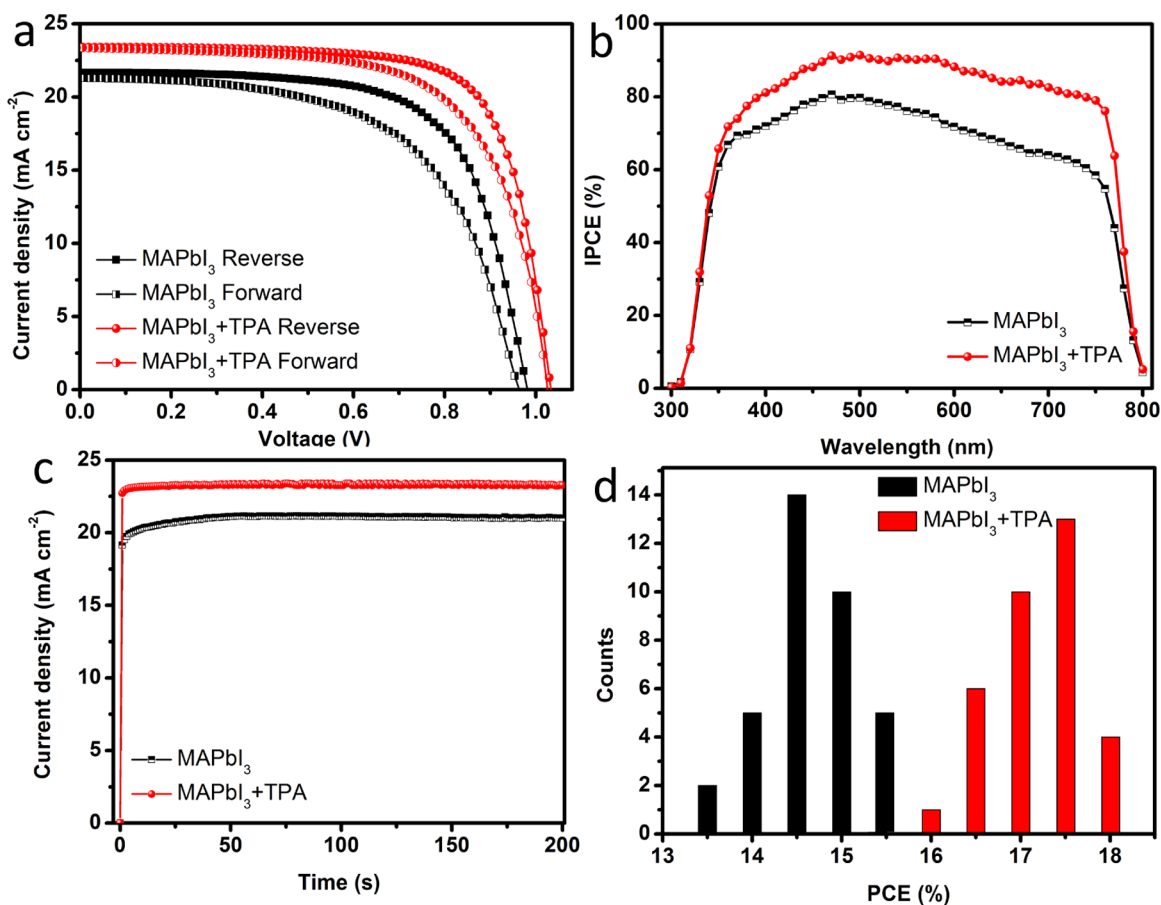


Figure 5. (a) *J*-*V* curves and (b) IPCE spectra of PSCs with pristine MAPbI₃ and MAPbI₃ with 10 mg mL⁻¹ TPA additive. (c) Time profiles of photocurrent density obtained by holding solar cells at bias voltage of 0.80 V. (d) PCE distributions of statistic 36 devices for each type of PSCs without and with TPA.

Table 2. Photovoltaic Parameters of PSCs without and with TPA

cells	scan direction	V_{OC} (V)	J_{SC} (mA cm ⁻²)	FF (%)	PCE (%)
MAPbI ₃	forward	0.98	21.69	60.97	12.96
	reverse	0.99	22.09	71.02	15.53
MAPbI ₃ + TPA	forward	1.03	23.35	66.01	15.87
	reverse	1.05	23.49	75.06	18.51

some mobile iodide ions in MAPbI₃ due to hydrogen-bonding interactions, which is beneficial to alleviate the J - V hysteresis phenomenon of PSCs.^{37,38}

The incident photon-to-electron conversion efficiency (IPCE) spectrum of PSCs with TPA compared to the pristine cell was obviously increased in the wavelength range of 350–780 nm, as shown in Figure 5b, which is attributed to better light absorption and charge transport and collection abilities. The integrated J_{SC} values calculated from the IPCE spectra for PSCs without and with TPA are 21.42 and 23.36 mA cm⁻², respectively, which are almost consistent with the values measured from the J - V curves.

To validate results, we have also recorded the steady-state current density of PSCs without and with TPA additive by holding the potential at about the maximum output point (0.8 V). As shown in Figure 5c, both PSCs with and without TPA quickly responded and their current densities stayed at about 23.33 and 21.72 mA cm⁻², respectively, which confirm the accuracy of our performance measurement. The good

reproducibility was exhibited by statistic 36 devices for each type of PSCs, as shown in the histograms of Figure 5d. The average PCE value for PSCs with TPA is about 17.45%, which is obviously higher than that of pristine PSCs (14.51%).

The photoluminescence (PL) emission intensity of perovskite film without electron transport layer (ETL) and/or hole transport layer (HTL) is primarily from the recombination of the excitons. As shown in Figure 6a, the significantly enhanced PL intensity for MAPbI₃ film with TPA compared to the pristine MAPbI₃ film indicates that the nonradiative carrier recombination has been effectively retarded because of less defects and high-quality crystallinity of MAPbI₃ with TPA,^{39,40} which have been supported by SEM and XRD analyses above.

Figure 6b shows the photocurrent density (J_{ph}) of PSCs without and with TPA additive. J_{ph} is defined as $J_{ph} = J_{light} - J_{dark}$ where J_{light} and J_{dark} are the current densities under 1 sun illumination and in the dark, respectively. The effective voltage (V_{eff}) is defined as $V_{eff} = V_0 - V_a$, where V_0 is the voltage at which $J_{ph} = 0$ and V_a is the applied bias voltage.²⁴ Noticeably, J_{ph} of two cells linearly increased with V_{eff} at the low V_{eff} range (<0.45 V) and gradually approached a saturated photocurrent (J_{sat}) at the high V_{eff} range. In general, J_{sat} correlates to the maximum exciton generation rate (G_{max}), exciton dissociation probability, and carrier transport and collection probability at the high- V_{eff} region. The relatively larger J_{sat} for PSCs with TPA additive indicates better light absorption for MAPbI₃ layer with TPA, which is supported by the absorption spectra in Figure 4a. Assuming that all photogenerated excitons for one cell are dissociated into free carriers at a high V_{eff} , J_{sat} is only limited by

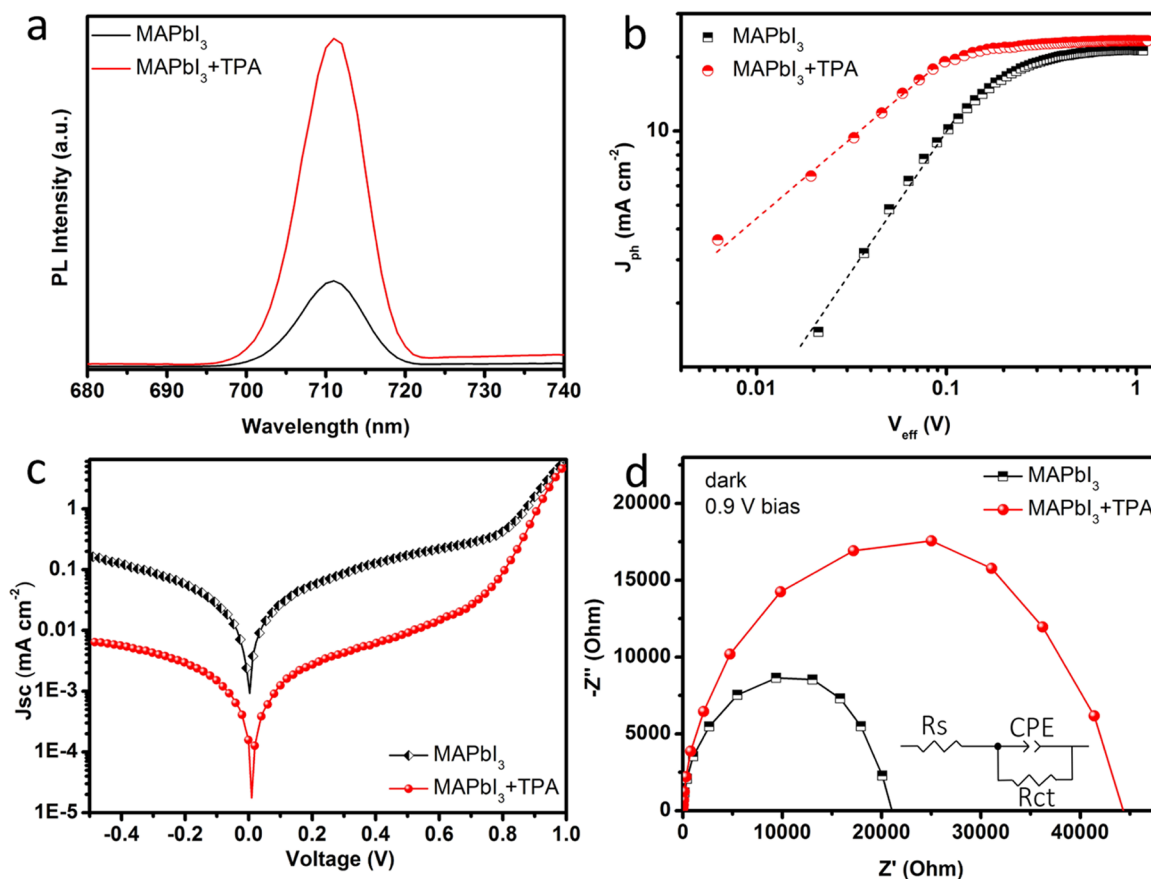


Figure 6. (a) Steady-state PL spectra of MAPbI₃ films without and with TPA. (b) J_{ph} - V_{eff} plots with double-logarithmic axis for PSCs without and with TPA. (c) Dark J - V curves for PSCs without and with TPA. (d) Nyquist plots of PSCs without and with TPA under dark condition.

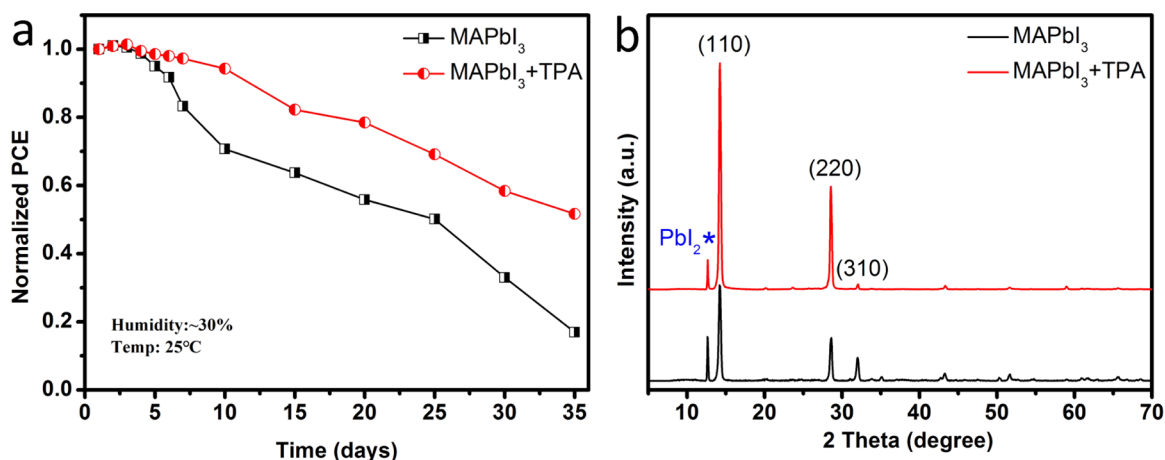


Figure 7. (a) Normalized PCE values of PSCs with aging time. (b) XRD patterns of perovskite films stored at room temperature in a 30% relative humidity for 35 days.

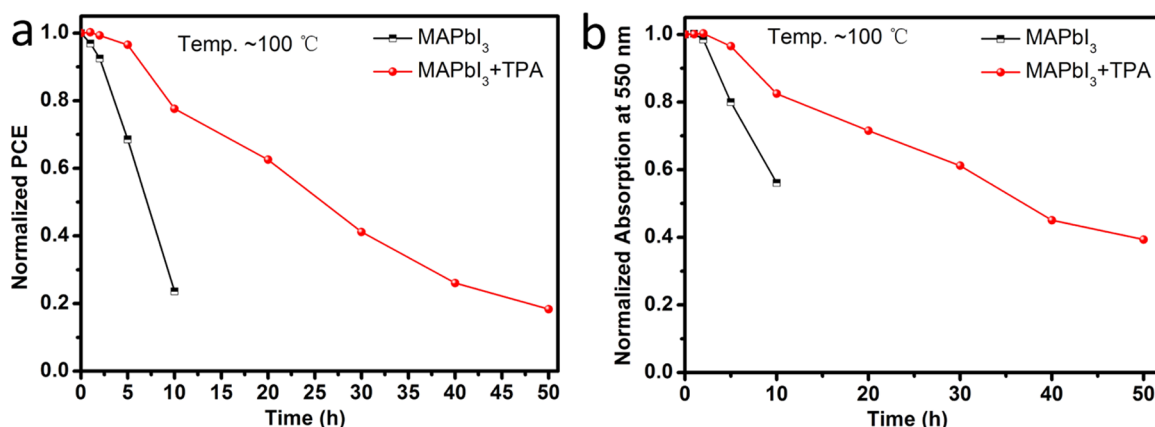


Figure 8. (a) Normalized PCE values of PSCs without and with TPA additive as a function of annealed time at 100 °C in N₂-filled glovebox. (b) Normalized light absorption intensities at 550 nm of the corresponding perovskite films with different annealing times.

the carrier transport and collection abilities. Therefore, carrier transport and collection probabilities at any V_{eff} can be directly obtained from the ratio $J_{\text{ph}}/J_{\text{sat}}$. The calculated carrier transport and collection probabilities of PSCs without and with TPA additive are 89.03 and 96.58%, respectively, indicating that cells with TPA additive have better carrier transport and collection abilities.

The enhanced performance of PSCs with TPA is further supported by the dark J - V characteristics, as shown in Figure 6c. The obviously lower reversed saturation current and higher rectification ratio of PSCs with TPA compared to pristine cells further demonstrate the reduced carrier recombination and the enhanced carrier transport and collection abilities. The reduced leakage current and carrier recombination current can contribute to improving the FF and V_{oc} of cells,^{40–42} which is consistent with the obtained higher values of FF and V_{oc} for PSCs with TPA additive.

Electrochemical impedance spectroscopy is a useful tool to investigate the interfacial charge transport and recombination behaviors in photovoltaic devices. Figure 6d presents the Nyquist plot measured in a frequency range of 0.1–10⁵ Hz at a forward bias voltage of 0.9 V under dark condition. A clear semicircle can be distinguished in the intermediate-frequency region for each type of cells, which is related to the charge transfer at FTO/ETL/MAPbI₃/HTL interfaces, mainly owing to the recombination of electrons.^{19,43} The recombination

resistances (R_{ct}) of PSCs with TPA are clearly larger than those of pristine PSCs, which further supports the superior performance of PSCs with TPA.

Due to their ionic character, metal halide perovskites are sensitive to moisture, and unsealed PSCs degrade rapidly in a humid environment.^{4,44} The time evolutions of PCE for PSCs without and with TPA derived from the J - V curves are shown in Figure 7a. The unsealed devices were stored in air with a relative humidity (RH) of 30%, and the pristine PSCs only kept 18% of the original PCE after 35 days, whereas PSCs with TPA additive still retained 51% of the original PCE value. Figure 7b exhibits the XRD patterns of MAPbI₃ films without and with TPA additive aging for 35 days. The peak at 12.7° is characteristic of the formation of the PbI₂ phase during the perovskite degradation process. The stronger intensity of PbI₂ peak indicates that the pristine MAPbI₃ film was severely corroded and produced more PbI₂ due to moisture invasion. An accelerated test of stability under high humidity (RH ~ 100%) was also performed, as shown in Figure S4. The PCEs of pristine PSCs and their absorption intensity of 550 nm became quickly invalid within 1 h, whereas the PSCs with TPA additive can resist for 2.5 h. Figure S5 shows the UV-vis absorption spectra of MAPbI₃ films without and with TPA additive exposed at RH ~ 100% for different times. The obviously stable absorption spectra of MAPbI₃ films with TPA additive further support that MAPbI₃ films with TPA additive show better

moisture resistance. The enhanced moisture resistance of MAPbI₃ films with TPA is possibly attributed to the compensative effects of the sheet-shaped perovskite covered onto the grain boundaries and the robust crystallization of perovskite film caused by TPA.^{16,45}

Thermal stability of PSCs is an important parameter as the cells have to undergo a heat test at 85 °C, and perovskite layer can be easily decomposed under such high temperature. Furthermore, the typical spiro-OMeTAD-based HTL would be quickly deteriorated due to accelerated diffusion of doped TBP and Li-TFSI under the heat test.⁴⁶ Therefore, MAPbI₃ photoactive layers with and without TPA additive were tested under a high temperature of 100 °C in a N₂-filled glovebox before spin-coating HTL to rule out the deterioration of spiro-OMeTAD. The PCEs of PSCs with and without TPA additive were decreased to 80 and 20% of the original PCEs, respectively, after heating for 10 h at 100 °C, as shown in Figure 8a. The attenuation of PSCs is mainly attributed to the decomposition of perovskite layer,^{47,48} which can be supported by the deterioration of the absorption intensity of perovskite films with annealing time, as shown in Figure 8b. The absorption intensity of MAPbI₃ films with TPA in the wavelength range of 450–600 nm is obviously stronger than that of pristine MAPbI₃ film after annealing at 100 °C for 10 h, as shown in Figure S6. The results indicate that the MAPbI₃ layer with TPA additive shows superior thermal stability due to the remarkable crystal morphology and the strong interaction between carboxyl group in TPA and perovskite grains.^{25,26}

CONCLUSIONS

The grains-interconnected perovskite film was obtained for the first time by incorporating TPA additive into perovskite precursor solution, which results in a morphology obviously different from that of the previously reported perovskite films. The right-concentration TPA additive can be enriched in the vicinity of crystal boundaries and grain surface, which can act as nucleation sites to form sheet-shaped perovskite covered onto the bottom grains. Therefore, some of the bottom perovskite grains were connected into communities, which can improve electrical interconnection between grains and reduce effects of grain boundaries. PSCs using TPA-induced interconnected perovskite grains exhibited a PCE of 18.51%, which is much higher than that of PSCs based on pristine MAPbI₃. PSCs without and with TPA additive kept 18 and 51% of the original PCEs, respectively, aging for 35 days at RH 30%, indicating that PSCs with TPA show better moisture resistance. Furthermore, PSCs with TPA still kept 80% of the original PCE value after annealing at 100 °C for 10 h, whereas the PCEs of pristine PSCs were almost decreased to 20% of the original PCE value, demonstrating that MAPbI₃ films with TPA additive have superior thermal stability. The remarkable morphology and superior crystallization of perovskite film caused by TPA additive are responsible for improved light absorption, carrier transportation, and collection probability, as well as superior thermal stability and moisture resistance of PSCs. This special morphology of perovskite layer would guide a direction to fabricate efficient and stable PSCs for commercial applications.

ASSOCIATED CONTENT

Supporting Information

The Supporting Information is available free of charge on the ACS Publications website at DOI: 10.1021/acsami.7b08488.

SEM images of perovskite films before annealing and without antisolvent treatment, cross-sectional SEM images of PSCs, stability test of PSCs under RH 100% or baked at 100 °C (PDF)

AUTHOR INFORMATION

Corresponding Author

*E-mail: xhchen@phy.ecnu.edu.cn.

ORCID

Xian Hou: 0000-0001-9436-3731

Sumei Huang: 0000-0001-5283-3918

Likun Pan: 0000-0001-9294-1972

Xiaohong Chen: 0000-0003-0018-0198

Notes

The authors declare no competing financial interest.

ACKNOWLEDGMENTS

This work was supported by the National Natural Science Foundation of China (61275038 and 11274119).

REFERENCES

- (1) Zhao, Y.; Zhu, K. Organic-Inorganic Hybrid Lead Halide Perovskites for Optoelectronic and Electronic Applications. *Chem. Soc. Rev.* **2016**, *45*, 655–689.
- (2) Zhu, W.; Yu, T.; Li, F.; Bao, C.; Gao, H.; Yi, Y.; Yang, J.; Fu, G.; Zhou, X.; Zou, Z. A Facile, Solvent Vapor-Fumigation-Induced, Self-Repair Recrystallization of CH₃NH₃PbI₃ Films for High-Performance Perovskite Solar Cells. *Nanoscale* **2015**, *7*, 5427–5434.
- (3) Chiang, C.-H.; Nazeeruddin, M. K.; Grätzel, M.; Wu, C.-G. The Synergistic Effect of H₂O and DMF Towards Stable and 20% Efficiency Inverted Perovskite Solar Cells. *Energy Environ. Sci.* **2017**, *10*, 808–817.
- (4) Sin, D. H.; Jo, S. B.; Lee, S. G.; Ko, H.; Kim, M.; Lee, H.; Cho, K. Enhancing the Durability and Carrier Selectivity of Perovskite Solar Cells Using a Blend Interlayer. *ACS Appl. Mater. Interfaces* **2017**, *9*, 18103–18112.
- (5) Williams, S. T.; Rajagopal, A.; Chueh, C.-C.; Jen, A. K.-Y. Current Challenges and Prospective Research for Upscaling Hybrid Perovskite Photovoltaics. *J. Phys. Chem. Lett.* **2016**, *7*, 811–819.
- (6) Numata, Y.; Kogo, A.; Udagawa, Y.; Kunugita, H.; Ema, K.; Sanehira, Y.; Miyasaka, T. Controlled Crystal Grain Growth in Mixed Cation-Halide Perovskite by Evaporated Solvent Vapor Recycling Method for High Efficiency Solar Cells. *ACS Appl. Mater. Interfaces* **2017**, *9*, 18739–18747.
- (7) Hou, X.; Xuan, T.; Sun, H.; Chen, X.; Li, H.; Pan, L. High-Performance Perovskite Solar Cells by Incorporating a ZnGa₂O₄: Eu³⁺ Nanophosphor in the Mesoporous TiO₂ Layer. *Sol. Energy Mater. Sol. Cells* **2016**, *149*, 121–127.
- (8) Yang, S.; Fu, W.; Zhang, Z.; Chen, H.; Li, C.-Z. Recent Advances in Perovskite Solar Cells: Efficiency, Stability and Lead-Free Perovskite. *J. Mater. Chem. A* **2017**, *5*, 11462–11482.
- (9) Best Research-Cell Efficiencies (NREL, 2016). <https://www.nrel.gov/pv/assets/images/efficiency-chart.png>.
- (10) Al-Dainy, G. A.; Bourdo, S. E.; Saini, V.; Berry, B. C.; Biris, A. S. Hybrid Perovskite Photovoltaic Devices: Properties, Architecture and Fabrication Methods. *Energy Technol.* **2017**, *5*, 373–401.
- (11) Zhao, Y.; Zhou, W.; Ma, W.; Meng, S.; Li, H.; Wei, J.; Fu, R.; Liu, K.; Yu, D.; Zhao, Q. Correlations between Immobilizing Ions and Suppressing Hysteresis in Perovskite Solar Cells. *ACS Energy Lett.* **2016**, *1*, 266–272.
- (12) Besleaga, C.; Abramiuc, L. E.; Stancu, V.; Tomulescu, A. G.; Sima, M.; Trinca, L.; Plugaru, N.; Pintilie, L.; Nemnes, G. A.; Iliescu, M.; et al. Iodine Migration and Degradation of Perovskite Solar Cells Enhanced by Metallic Electrodes. *J. Phys. Chem. Lett.* **2016**, *7*, 5168–5175.

- (13) Nie, W.; Tsai, H.; Asadpour, R.; Blancon, J.-C.; Neukirch, A. J.; Gupta, G.; Crochet, J. J.; Chhowalla, M.; Tretiak, S.; Alam, M. A.; et al. High-Efficiency Solution-Processed Perovskite Solar Cells with Millimeter-Scale Grains. *Science* **2015**, *347*, 522–525.
- (14) Li, D.; Liao, P.; Shai, X.; Huang, W.; Liu, S.; Li, H.; Shen, Y.; Wang, M. Recent Progress on Stability Issues of Organic-Inorganic Hybrid Lead Perovskite-Based Solar Cells. *RSC Adv.* **2016**, *6*, 89356–89366.
- (15) You, J.; Yang, Y.; Hong, Z.; Song, T.-B.; Meng, L.; Liu, Y.; Jiang, C.; Zhou, H.; Chang, W.-H.; Li, G.; Yang, Y. Moisture Assisted Perovskite Film Growth for High Performance Solar Cells. *Appl. Phys. Lett.* **2014**, *105*, No. 183902.
- (16) Xiao, Z.; Dong, Q.; Bi, C.; Shao, Y.; Yuan, Y.; Huang, J. Solvent Annealing of Perovskite-Induced Crystal Growth for Photovoltaic-Device Efficiency Enhancement. *Adv. Mater.* **2014**, *26*, 6503–6509.
- (17) Hao, F.; Stoumpos, C. C.; Liu, Z.; Chang, R. P.; Kanatzidis, M. G. Controllable Perovskite Crystallization at a Gas-Solid Interface for Hole Conductor-Free Solar Cells with Steady Power Conversion Efficiency over 10%. *J. Am. Chem. Soc.* **2014**, *136*, 16411–16419.
- (18) Zhou, Z.; Wang, Z.; Zhou, Y.; Pang, S.; Wang, D.; Xu, H.; Liu, Z.; Padture, N. P.; Cui, G. Methylamine-Gas-Induced Defect-Healing Behavior of $\text{CH}_3\text{NH}_3\text{PbI}_3$ Thin Films for Perovskite Solar Cells. *Angew. Chem., Int. Ed.* **2015**, *54*, 9705–9709.
- (19) Zhu, W.; Bao, C.; Wang, Y.; Li, F.; Zhou, X.; Yang, J.; Lv, B.; Wang, X.; Yu, T.; Zou, Z. Coarsening of One-Step Deposited Organolead Triiodide Perovskite Films via Ostwald Ripening for High Efficiency Planar-Heterojunction Solar Cells. *Dalton Trans.* **2016**, *45*, 7856–7865.
- (20) Liang, P. W.; Liao, C. Y.; Chueh, C. C.; Zuo, F.; Williams, S. T.; Xin, X. K.; Lin, J.; Jen, A. K. Y. Additive Enhanced Crystallization of Solution-Processed Perovskite for Highly Efficient Planar-Heterojunction Solar Cells. *Adv. Mater.* **2014**, *26*, 3748–3754.
- (21) Li, X.; Dar, M. I.; Yi, C.; Luo, J.; Tschumi, M.; Zakeeruddin, S. M.; Nazeeruddin, M. K.; Han, H.; Grätzel, M. Improved Performance and Stability of Perovskite Solar Cells by Crystal Crosslinking with Alkylphosphonic Acid ω -ammonium Chlorides. *Nat. Chem.* **2015**, *7*, 703–711.
- (22) Li, B.; Fei, C.; Zheng, K.; Qu, X.; Pullerits, T.; Cao, G.; Tian, J. Constructing Water-Resistant $\text{CH}_3\text{NH}_3\text{PbI}_3$ Perovskite Films via Coordination Interaction. *J. Mater. Chem. A* **2016**, *4*, 17018–17024.
- (23) Bi, D.; Yi, C.; Luo, J.; Décoppet, J.-D.; Zhang, F.; Zakeeruddin, S. M.; Li, X.; Hagfeldt, A.; Grätzel, M. Polymer-Templated Nucleation and Crystal Growth of Perovskite Films for Solar Cells with Efficiency Greater than 21%. *Nat. Energy* **2016**, *1*, 16142.
- (24) Zhao, Y.; Wei, J.; Li, H.; Yan, Y.; Zhou, W.; Yu, D.; Zhao, Q. A Polymer Scaffold for Self-Healing Perovskite Solar Cells. *Nat. Commun.* **2016**, *7*, No. 10228.
- (25) Masi, S.; Rizzo, A.; Munir, R.; Listorti, A.; Giuri, A.; Corcione, C. E.; Treat, N. D.; Gigli, G.; Amassian, A.; Stingelin, N.; et al. Organic Gelators as Growth Control Agents for Stable and Reproducible Hybrid Perovskite-Based Solar Cells. *Adv. Energy Mater.* **2017**, *7*, No. 1602600.
- (26) Fu, R.; Zhao, Y.; Li, Q.; Zhou, W.; Yu, D.; Zhao, Q. Enhanced Long-Term Stability of Perovskite Solar Cells by 3-hydroxypyridine Dipping. *Chem. Commun.* **2017**, *53*, 1829–1831.
- (27) Dualeh, A.; Gao, P.; Seok, S.; Il; Nazeeruddin, M. K.; Grätzel, M. Thermal Behavior of Methylammonium Lead-Trihalide Perovskite Photovoltaic Light Harvesters. *Chem. Mater.* **2014**, *26*, 6160–6164.
- (28) Lin, Z. H.; Chang, J. J.; Zhu, H.; Xu, Q. H.; Zhang, C. F.; Ouyang, J. Y.; Hao, Y. Enhanced Planar Heterojunction Perovskite Solar Cell Performance and Stability using PDDA Polyelectrolyte Capping Agent. *Sol. Energy Mater. Sol. Cells* **2017**, *172*, 133–139.
- (29) Reche-Tamayo, M.; Moral, M.; Pérez-Jiménez, A. J.; Sancho-García, J. C. Theoretical Determination of Interaction and Cohesive Energies of Weakly Bound Cycloparaphenylene Molecules. *J. Phys. Chem. C* **2016**, *120*, 22627–22634.
- (30) Steemers, L.; Wanner, M. J.; Ehlers, A. W.; Hiemstra, H.; Marseveen, J. H. V. A Short Covalent Synthesis of an All-Carbon-Ring [2]Rotaxane. *Org. Lett.* **2017**, *19*, 2342–2345.
- (31) Cacciuto, A.; Auer, S.; Frenkel, D. Onset of Heterogeneous Crystal Nucleation in Colloidal Suspensions. *Nature* **2004**, *428*, 404–406.
- (32) Ahn, N.; Son, D.-Y.; Jang, I.-H.; Kang, S. M.; Choi, M.; Park, N.-G. Highly Reproducible Perovskite Solar Cells with Average Efficiency of 18.3% and Best Efficiency of 19.7% Fabricated via Lewis base Adduct of Lead (II) Iodide. *J. Am. Chem. Soc.* **2015**, *137*, 8696–8699.
- (33) Lin, Q.; Armin, A.; Nagiri, R. C. R.; Burn, P. L.; Meredith, P. Electro-Optics of Perovskite Solar Cells. *Nat. Photonics* **2014**, *9*, 106–112.
- (34) Hou, X.; Pan, L.; Huang, S.; Wei, O.-Y.; Chen, X. Enhanced Efficiency and Stability of Perovskite Solar Cells using Porous Hierarchical TiO_2 Nanostructures of Scattered Distribution as Scaffold. *Electrochim. Acta* **2017**, *236*, 351–358.
- (35) Paek, S.; Schouwink, P.; Nefeli Athanasopoulou, E.; Cho, K. T.; Grancini, G.; Lee, Y.; Zhang, Y.; Stellacci, F.; Nazeeruddin, M. K.; Gao, P. From Nano- to Micrometer Scale: The Role of Antisolvent Treatment on High Performance Perovskite Solar Cells. *Chem. Mater.* **2017**, *29*, 3490–3498.
- (36) Sanchez, R. S.; Gonzalez-Pedro, V.; Lee, J.-W.; Park, N.-G.; Kang, Y. S.; Mora-Sero, I.; Bisquert, J. Slow Dynamic Processes in Lead Halide Perovskite Solar Cells. Characteristic Times and Hysteresis. *J. Phys. Chem. Lett.* **2014**, *5*, 2357–2363.
- (37) Chen, B.; Yang, M.; Zheng, X.; Wu, C.; Li, W.; Yan, Y.; Bisquert, J.; Garcia-Belmonte, G.; Zhu, K.; Priya, S. Impact of Capacitive Effect and Ion Migration on the Hysteretic Behavior of Perovskite Solar Cells. *J. Phys. Chem. Lett.* **2015**, *6*, 4693–4700.
- (38) Chen, B.; Yang, M.; Priya, S.; Zhu, K. Origin of J-V Hysteresis in Perovskite Solar Cells. *J. Phys. Chem. Lett.* **2016**, *7*, 905–917.
- (39) Xiang, W.; Chen, Q.; Wang, Y.; Liu, M.; Huang, F.; Bu, T.; Wang, T.; Cheng, Y.-B.; Gong, X.; Zhong, J.; et al. Improved Air Stability of Perovskite Hybrid Solar Cells via Blending Poly(dimethylsiloxane)-urea Copolymers. *J. Mater. Chem. A* **2017**, *5*, 5486–5494.
- (40) Luo, H.; Lin, X.; Hou, X.; Pan, L.; Huang, S.; Chen, X. Efficient and Air-Stable Planar Perovskite Solar Cells Formed on Graphene-Oxide-Modified PEDOT:PSS Hole Transport Layer. *Nano-Micro Lett.* **2017**, *9*, 39.
- (41) Jiang, Z.; Chen, X.; Lin, X.; Jia, X.; Wang, J.; Pan, L.; Huang, S.; Zhu, F.; Sun, Z. Amazing Stable Open-Circuit Voltage in Perovskite Solar Cells using AgAl Alloy Electrode. *Sol. Energy Mater. Sol. Cells* **2016**, *146*, 35–43.
- (42) Li, B.; Zheng, C.; Liu, H.; Zhu, J.; Zhang, H.; Gao, D.; Huang, W. Large Planar π -Conjugated Porphyrin for Interfacial Engineering in p-i-n Perovskite Solar Cells. *ACS Appl. Mater. Interfaces* **2016**, *8*, 27438–27443.
- (43) Zhu, L.; Shi, J.; Lv, S.; Yang, Y.; Xu, X.; Xu, Y.; Xiao, J.; Wu, H.; Luo, Y.; Li, D.; et al. Temperature-Assisted Controlling Morphology and Charge Transport Property for Highly Efficient Perovskite Solar Cells. *Nano Energy* **2015**, *15*, 540–548.
- (44) Han, Y.; Meyer, S.; Dkhissi, Y.; Weber, K.; Pringle, J. M.; Bach, U.; Spiccia, L.; Cheng, Y.-B. Degradation Observations of Encapsulated Planar $\text{CH}_3\text{NH}_3\text{PbI}_3$ Perovskite Solar Cells at High Temperatures and Humidity. *J. Mater. Chem. A* **2015**, *3*, 8139–8147.
- (45) Xu, T.; Chen, L.; Guo, Z.; Ma, T. Strategic Improvement of the Long-Term Stability of Perovskite Materials and Perovskite Solar Cells. *Phys. Chem. Chem. Phys.* **2016**, *18*, 27026–27050.
- (46) Pellaroque, A.; Noel, N. K.; Habisreutinger, S. N.; Zhang, Y. D.; Barlow, S.; Marder, S. R.; Snaith, H. J. Efficient and Stable Perovskite Solar Cells Using Molybdenum Tris(dithiolene)s as p-Dopants for Spiro-OMeTAD. *ACS Energy Lett.* **2017**, *2*, 2044–2050.
- (47) Niu, G.; Guo, X.; Wang, L. Review of Recent Progress in Chemical Stability of Perovskite Solar Cells. *J. Mater. Chem. A* **2015**, *3*, 8970–8980.
- (48) Lee, J. W.; Kim, D. H.; Kim, H. S.; Seo, S. W.; Cho, S. M.; Park, N. G. Formamidinium and Cesium Hybridization for Photo- and Moisture-Stable Perovskite Solar Cell. *Adv. Energy Mater.* **2015**, *5*, No. 1501310.